

THREE-DIMENSIONAL RELATIVISTIC PAIR PLASMA RECONNECTION WITH RADIATIVE FEEDBACK IN THE CRAB NEBULA

B. CERUTTI^{1,2,3}, G. R. WERNER³, D. A. UZDENSKY³ & M. C. BEGELMAN^{4,5}

¹Department of Astrophysical Sciences, Princeton University, Princeton, NJ 08544, USA; bcerutti@astro.princeton.edu

²Lyman Spitzer Jr. Fellow

³Center for Integrated Plasma Studies, Physics Department, University of Colorado, UCB 390, Boulder, CO 80309-0390, USA; greg.werner@colorado.edu, uzdensky@colorado.edu

⁴JILA, University of Colorado and National Institute of Standards and Technology, UCB 440, Boulder, CO 80309-0440, USA; mitch@jila.colorado.edu and

⁵Department of Astrophysical and Planetary Sciences, University of Colorado, UCB 391, Boulder, CO 80309-0391, USA

Draft version October 30, 2018

ABSTRACT

The discovery of rapid synchrotron gamma-ray flares above 100 MeV from the Crab Nebula has attracted new interest in alternative particle acceleration mechanisms in pulsar wind nebulae. Diffuse shock-acceleration fails to explain the flares because particle acceleration and emission occur during a single or even sub-Larmor timescale. In this regime, the synchrotron energy losses induce a drag force on the particle motion that balances the electric acceleration and prevents the emission of synchrotron radiation above 160 MeV. Previous analytical studies and 2D particle-in-cell (PIC) simulations indicate that relativistic reconnection is a viable mechanism to circumvent the above difficulties. The reconnection electric field localized at X-points linearly accelerates particles with little radiative energy losses. In this paper, we check whether this mechanism survives in 3D, using a set of large PIC simulations with radiation reaction force and with a guide field. In agreement with earlier works, we find that the relativistic drift kink instability deforms and then disrupts the layer, resulting in significant plasma heating but few non-thermal particles. A moderate guide field stabilizes the layer and enables particle acceleration. We report that 3D magnetic reconnection can accelerate particles above the standard radiation reaction limit, although the effect is less pronounced than in 2D with no guide field. We confirm that the highest energy particles form compact bunches within magnetic flux ropes, and a beam tightly confined within the reconnection layer, which could result in the observed Crab flares when, by chance, the beam crosses our line of sight.

Subject headings: Acceleration of particles — Magnetic reconnection — Radiation mechanisms: non-thermal — ISM: individual (Crab Nebula)

1. INTRODUCTION

The non-thermal radiation emitted in pulsar wind nebulae is commonly associated with ultra-relativistic electron-positron pairs injected by the pulsar and accelerated at the termination shock. In the Crab Nebula, the particle spectrum above ~ 1 TeV responsible for the X-ray to gamma-ray synchrotron emission is well modeled by a single power-law distribution of index -2.2 , which is usually associated with first-order Fermi acceleration at the shock front (see e.g., Kirk et al. 2009). Since the detections of the first flares of high-energy gamma rays in 2010 (Abdo et al. 2011; Tavani et al. 2011; Balbo et al. 2011) and the following ones detected since then (Striani et al. 2011; Buehler et al. 2012; Striani et al. 2013; Mayer et al. 2013; Buson et al. 2013), we know that the Crab Nebula occasionally accelerates particles up to a few 10^{15} eV (see reviews by Arons 2012 and Buehler & Blandford 2013). This discovery is very puzzling because the particles are accelerated to such energies within a few days, which corresponds to their Larmor gyration time in the Nebula. This is far too fast for Fermi-type acceleration mechanisms which operate over multiple crossings of the particles through the shock (e.g., Blandford & Eichler 1987). In addition, the observed particle spectrum is very hard, which is not compatible with the steep power-law $\gtrsim 2$ expected with diffuse shock-acceleration (Buehler et al. 2012). Even more surprising, the particles emit synchrotron radiation above the well-established radiation reaction limit photon energy of 160 MeV (Guilbert et al. 1983; de Jager et al. 1996; Lyutikov 2010;

Uzdensky et al. 2011). It implies that the particles must be subject to extreme synchrotron cooling over a sub-Larmor timescale. Hence, in principle, synchrotron cooling should prevent the acceleration of pairs to such high energies in the first place.

Fortunately, there is a simple way to circumvent these tight constraints on particle acceleration if there is a region of strong coherent electric field associated with a low magnetic field perpendicular to the particle motion, i.e., if $E > B_{\perp}$. This supposes that a non-ideal, dissipative magnetohydrodynamic process is at work somewhere in the Nebula. Using a simple semi-analytical approach, Uzdensky et al. (2011) and Cerutti et al. (2012a) showed that such extreme particle acceleration can occur within a Sweet-Parker-like reconnection layer (Parker 1957; Sweet 1958; Zweibel & Yamada 2009), where the reversing reconnecting magnetic field traps and confines the highest energy particles deep inside the layer where $E > B_{\perp}$ (Speiser 1965; Kirk 2004; Contopoulos 2007). The reconnection electric field accelerates the particles almost linearly along a few light-day long layer. This solution solves the sub-Larmor acceleration problem at the same time. Two-dimensional (2D) particle-in-cell (PIC) simulations of relativistic pair plasma reconnection with radiation reaction force have confirmed and strengthened the viability of this scenario (Cerutti et al. 2013). These simulations can also explain the observed rapid intra-flare time variability of the > 160 MeV synchrotron flux, the apparent photon spectral shape, as well as the flux/cutoff energy correlation (Buehler et al. 2012).

Although these 2D PIC simulations provide a fairly complete assessment of extreme particle acceleration in reconnection layers, it is still a simplified picture of a truly three-dimensional process. We know from previous 3D reconnection studies (Zenitani & Hoshino 2005, 2008; Daughton et al. 2011; Liu et al. 2011; Sironi & Spitkovsky 2011; Kagan et al. 2013; Markidis et al. 2013) that the reconnection layer is unstable to the relativistic tearing and kink modes, and a combination of these two into oblique modes. The kink (and oblique) instabilities, which cannot arise in the 2D simulations of Cerutti et al. (2013), can lead to significant deformation or even disruption of the reconnection layer in 3D simulations, subsequently suppressing particle acceleration. However, a moderate guide magnetic field can stabilize the layer (Zenitani & Hoshino 2005, 2007, 2008; Sironi & Spitkovsky 2011).

In this work, we extend the previous 2D study of Cerutti et al. (2013) by performing large 3D PIC simulations of pair plasma reconnection with radiative feedback and with guide field, in the context of the Crab flares. In the next section, we first present the numerical techniques and the setup of the simulations chosen for this study. Then, we investigate separately the effect of the tearing and the kink instabilities on the efficiency of particle acceleration, using a set of 2D simulations in Section 3. In Section 4, we establish the conditions for particle acceleration above the radiation reaction limit and emission of > 160 MeV synchrotron radiation in 3D reconnection. In addition, we report in this section on strong anisotropy and inhomogeneity of the highest-energy particles in 3D reconnection consistent with 2D results, and their important role in explaining the observed *Fermi*-LAT gamma-ray flux of the Crab flares. We summarize and discuss the results of this work in Section 5.

2. NUMERICAL APPROACH AND SIMULATION SETUP

2.1. Numerical techniques

All the simulations presented in this work were performed with *Zeltron*¹, a parallel three-dimensional electromagnetic PIC code (Cerutti et al. 2013). *Zeltron* solves self-consistently Maxwell’s equations using the Yee finite-difference time-domain (FDTD) algorithm (Yee 1966), and Newton’s equation following the Boris FDTD algorithm (Birdsall & Langdon 2005). Unlike most PIC codes, *Zeltron* includes the effect of the radiation reaction force in Newton’s equation (or the so-called “Lorentz-Abraham-Dirac equation”) induced by the emission of radiation by the particles (see also, e.g., Jaroschek & Hoshino 2009; Tamburini et al. 2010; Capdessus et al. 2012). In the ultra-relativistic regime, the radiation reaction force, \mathbf{g} , is akin to a continuous friction force, proportional to the radiative power and opposite to the particle’s direction of motion (e.g., Landau & Lifshitz 1975; Tamburini et al. 2010; Cerutti et al. 2012a). The expression of the radiation reaction force used in *Zeltron* is given by

$$\mathbf{g} = -\frac{2}{3}r_e^2\gamma \left[\left(\mathbf{E} + \frac{\mathbf{u} \times \mathbf{B}}{\gamma} \right)^2 - \left(\frac{\mathbf{u} \cdot \mathbf{E}}{\gamma} \right)^2 \right] \mathbf{u}, \quad (1)$$

where $r_e \approx 2.82 \times 10^{-13}$ cm is the classical radius of the electron, γ is the Lorentz factor of the particle, \mathbf{E} and \mathbf{B} are the electric and magnetic fields, and $\mathbf{u} = \gamma\mathbf{v}/c$ is the four-velocity divided by the speed of light. This formulation is valid if

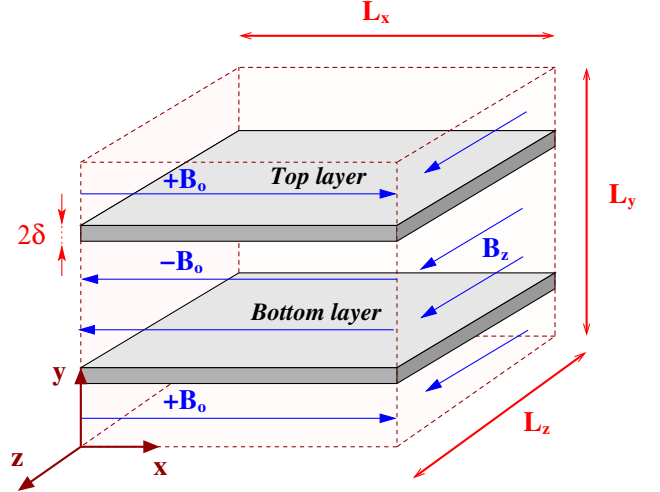


FIG. 1.— Initial simulation setup and geometry. The computational domain is a rectangular box of volume $L_x \times L_y \times L_z$ with periodic boundary conditions in all directions. The box initially contains two flat, anti-parallel, relativistic Harris layers in the xz -plane centered at $y = L_y/4$ and $y = 3L_y/4$, of some thickness 2δ . The magnetic field structure is composed of the reconnecting field, B_0 , along the x -direction, which reverses across the layers, and a uniform guide field, $B_z = \alpha B_0$, along the z -direction.

$\gamma B/B_{\text{QED}} \ll 1$, where $B_{\text{QED}} = 4.4 \times 10^{13}$ G is the quantum critical magnetic field. Because of the relativistic effects, the typical frequency of the expected radiation is $\sim \gamma^3 \gg 1$ times the relativistic cyclotron frequency. Hence, the radiation is not resolved by the grid and time step of the simulation. It must be calculated separately. *Zeltron* computes the emitted optically thin radiation (spectrum, and angular distributions) assuming it is pure synchrotron radiation. This is valid if the change of the particle energy is small, $\Delta\gamma/\gamma \ll 1$, during the formation length of a synchrotron photon, given by the relativistic Larmor radius divided by γ . We checked *a posteriori* that this assumption is indeed correct. The code also models the inverse Compton drag force on the particle motion in an imposed photon field, but this effect is negligible in the context of the Crab flares (Cerutti et al. 2012a), hence this capability will not be utilized in the following. To perform the large 3D simulations presented in this paper, *Zeltron* ran on 97,200 cores on the Kraken supercomputer² with nearly perfect scaling.

2.2. Simulation setup

The simulation setup chosen here is almost identical to our previous two-dimensional pair plasma reconnection simulations with radiation reaction force in Cerutti et al. (2013). The computational domain is a rectangular box of dimensions L_x , L_y and L_z , respectively along the x -, y - and z -directions, with periodic boundary conditions in all directions. We set up the simulation with two flat anti-parallel relativistic Harris current layers (Kirk & Skjæraasen 2003) in the xz -plane located at $y = L_y/4$ and $y = 3L_y/4$ (Figure 1). Having two current sheets is only a convenient numerical artifact that allows us to use periodic boundary conditions along the y -direction, but it does not have a physical meaning in the context of our model of the Crab flares where only one reconnection layer is involved. The electric current, J_z , flows in the $\pm z$ -directions, and is

¹ <http://benoit.cerutti.free.fr/zeltron.html>

² National Institute for Computational Sciences (www.nics.tennessee.edu/).

TABLE I
 COMPLETE LIST OF THE NUMERICAL SIMULATIONS PRESENTED IN THIS PAPER

Name simulation	L_x/ρ_0	L_y/ρ_0	L_z/ρ_0	Grid cells	# particles	α
2DXY0	200	200	—	1440 ²	3.32×10^7	0
2DXY025	200	200	—	1440 ²	3.32×10^7	0.25
2DXY050	200	200	—	1440 ²	3.32×10^7	0.5
2DXY075	200	200	—	1440 ²	3.32×10^7	0.75
2DXY1	200	200	—	1440 ²	3.32×10^7	1
2DYZ0	—	200	200	1440 ²	3.32×10^7	0
2DYZ025	—	200	200	1440 ²	3.32×10^7	0.25
2DYZ040	—	200	200	1440 ²	3.32×10^7	0.4
2DYZ050	—	200	200	1440 ²	3.32×10^7	0.5
2DYZ060	—	200	200	1440 ²	3.32×10^7	0.6
2DYZ075	—	200	200	1440 ²	3.32×10^7	0.75
2DYZ1	—	200	200	1440 ²	3.32×10^7	1
3D0	200	200	200	1440 ³	4.78×10^{10}	0
3D050	200	200	200	1440 ³	4.78×10^{10}	0.5

NOTE. — There are three distinct subsets of simulations. The first subset comprises 5 2D simulations of reconnection in the xy -plane, designed to study the effect of the guide field strength α on the dynamics of reconnection and particle acceleration. The second subset comprises 7 2D simulations of the reconnection layer in the yz -plane, in order to study the development of the kink instability as a function of the guide field strength α . The last set of simulations is chosen to test particle acceleration beyond the radiation reaction limit in 3D, in the best and in the worst cases identified in the 2D subsets.

supported by electrons counter-streaming with positrons at a mildly relativistic drift velocity (relative to the speed of light) $\beta_{\text{drift}} = 0.6$. The plasma (electrons and positrons) is spatially distributed throughout the domain, with the following density profile

$$n = \begin{cases} n_0 \left[\cosh\left(\frac{y-L_y/4}{\delta}\right) \right]^{-2} + 0.1n_0 & \text{if } y < L_y/2 \\ n_0 \left[\cosh\left(\frac{y-3L_y/4}{\delta}\right) \right]^{-2} + 0.1n_0 & \text{if } y > L_y/2 \end{cases}. \quad (2)$$

The first term is the density of the drifting pairs carrying the initial current, concentrated within the layer half-thickness $\delta = \lambda_D/\beta_{\text{drift}}$, where λ_D is the relativistic Debye length (Kirk & Skjæraasen 2003). This population is modeled with a uniform and isotropic (in the co-moving frame) distribution of macro-particles with variable weights to account for the density profile and to decrease the numerical noise in low-density regions. The second term is a uniform and isotropic background pair plasma at rest in the laboratory frame with a density chosen to be 10 times lower than at the center of the layers (i.e., $0.1n_0$). The drifting and the background particles are distributed in energy according to a relativistic Maxwellian with the same temperature $\theta_0 \equiv kT/m_e c^2 = 10^8$, where k is the Boltzmann constant and m_e is the rest mass of the electron. The temperature of the drifting particles is defined in the co-moving frame. This temperature models the ultra-relativistic plasma already present in the Crab Nebula, prior to reconnection, whose particles could have been accelerated at the wind termination shock or even by other reconnection events throughout the nebula. However, observations show that in reality the background plasma is distributed according to a broad and steep power-law, extending roughly between $\gamma_{\text{min}} = 10^6$ and $\gamma_{\text{max}} = 10^9$ (responsible for the UV to 100 MeV synchrotron spectrum). This large dynamic range of particle energies translates directly into an equally large dynamic range of relativistic Larmor radii and hence of length scales that must be resolved in the simulation, which is beyond the reach of our numerical capabilities.

The initial electromagnetic field configuration is

$$\mathbf{B} = \begin{cases} -B_0 \tanh\left(\frac{y-L_y/4}{\delta}\right) \mathbf{e}_x + \alpha B_0 \mathbf{e}_z & \text{if } y < L_y/2 \\ B_0 \tanh\left(\frac{y-3L_y/4}{\delta}\right) \mathbf{e}_x + \alpha B_0 \mathbf{e}_z & \text{if } y > L_y/2 \end{cases}, \quad (3)$$

$$\mathbf{E} = \mathbf{0}, \quad (4)$$

where \mathbf{e}_x , \mathbf{e}_z are unit vectors along the x - and z -directions. B_0 is the upstream reconnecting magnetic field and α is a dimensionless parameter of the simulation that quantifies the strength of the guide field component B_z in units of B_0 (Figure 1). Observations constrain the magnetic field in the emitting region to about 1 mG, which is much higher than the expected average quiescent field of order 100-200 μG (Meyer et al. 2010). In this work, we choose $B_0 = 5$ mG to be consistent with our previous studies of the flares (Cerutti et al. 2012a, 2013). Hence, the energy scale at which the radiation reaction force equals the electric force, assuming that $E = B_0 = 5$ mG, is

$$\gamma_{\text{rad}} m_e c^2 = \sqrt{\frac{3em_e^2 c^4}{2r_e^2 B_0}} \approx 1.3 \times 10^9 m_e c^2, \quad (5)$$

where e is the fundamental electric charge. Below, we express lengths in units of the typical initial Larmor radius of the particles in the simulations, i.e., $\rho_0 = \theta_0 m_e c^2 / e B_0 \approx 3.4 \times 10^{13}$ cm. In all the simulations, the layer half-thickness is then $\delta/\rho_0 \approx 2.7$ and the relativistic collisionless electron skin-depth $d_e \equiv \sqrt{\theta_0 m_e c^2 / 4\pi n_0 e^2} \approx 1.8\rho_0$. Similarly, timescales are given in units of the gyration time of the bulk of the particles in the plasma, i.e., $\omega_0^{-1} \equiv \rho_0/c \approx 1140$ s. The initial distribution of fields and plasma results in a low plasma- β or high magnetization of the upstream plasma (i.e., outside the layers). Here, the magnetization parameter is $\sigma \equiv B_0^2 / 4\pi(0.1n_0)\theta_0 m_e c^2 \approx 16$.

The system is initially set at an equilibrium, i.e., there is a force balance across the reconnection layers between the magnetic pressure and the drifting particle pressure. This equilibrium is unstable to two competing instabilities, namely the relativistic tearing and kink instabilities, as well as oblique modes that combine tearing and kink modes (Zenitani & Hoshino 2005, 2008; Daughton et al. 2011; Kagan et al.

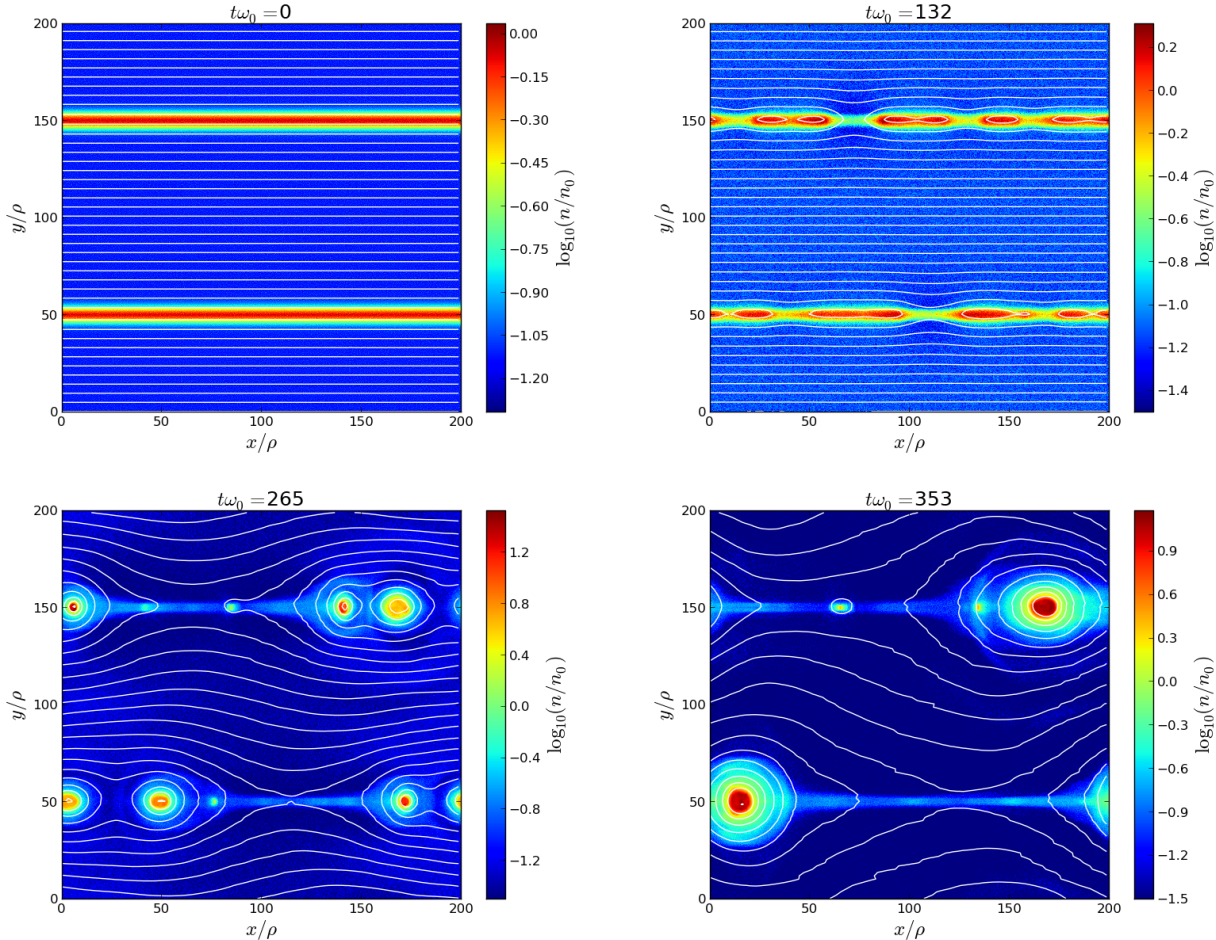


FIG. 2.— Snapshots of the plasma density at $t\omega_0 = 0$ (top left), 132 (top right), 265 (bottom left), and 353 (bottom right) of the 2D simulation 2DXY0 in the xy -plane (with no guide field, $\alpha = 0$). Magnetic field lines are represented by solid white lines. In this simulation, the development of the tearing instability forms multiple plasmoids separated by X-points which facilitates fast magnetic reconnection. Reconnection dissipates about 70% of the magnetic energy in the form of energetic particles and radiation (see Figures 6-7).

2013). In contrast to Cerutti et al. (2013), we choose here not to apply any initial perturbation in order to avoid any artificial enhancement of one type of instability over the other. Instabilities are seeded with the numerical noise only. This choice has a direct computational cost because the lack of perturbation significantly delays the onset of reconnection (See Sections 3.1, 4.1), but it enables a fair comparison between the growth rates of both instabilities (Sections 3.2, 4.2). Another important consequence of this choice specific to this study is the significant radiative cooling of the particles before reconnection can accelerate them (Section 3.3).

2.3. Set of simulations

In this work, we performed a series of 14 simulations. This set includes 12 2D simulations, and 2 3D simulations. The 2D simulations are designed to study the effect of the guide field strength, $\alpha = 0, 0.25, 0.5, 0.75$ and 1 on the developments of instabilities (kink and tearing) and on particle acceleration/emission. To analyze the developments both instabilities separately, we follow the same approach as Zenitani & Hoshino (2007, 2008), i.e., we consider the dynamics of the Harris current layers in the xy -plane where the tearing modes alone develop similarly to our previous study in Cerutti et al. (2013), and in the yz -plane where the kink modes alone develop (the kink and the tearing modes are

perpendicular to each other). The box is square of size $L_x \times L_y = (200\rho_0)^2$ and $L_y \times L_z = (200\rho_0)^2$ with 1440^2 cells and 16 particles per cell (all species together). The spatial resolution is $\rho_0/\Delta x \approx 7.2$, where Δx is the grid spacing in the x -direction ($\Delta x = \Delta y = \Delta z$), which ensures the conservation of the total energy to within $\lesssim 1\%$ error throughout the simulation. From this 2D scan, we identify the best/worst conditions for efficient particle acceleration and emission above the radiation reaction limit in 3D. The 3D box is cubical of size $L_x \times L_y \times L_z = (200\rho_0)^3$ with 1440^3 grid cells and 16 particles per cell (all species together). The simulation time step is set at 0.3 times the critical Courant-Friedrichs-Lewy time step, $\Delta t = 0.3\Delta t_{\text{CFL}} \approx 0.029\omega_0^{-1}$ in 2D and $\approx 0.024\omega_0^{-1}$ in 3D, in order to maintain satisfactory total energy conservation in the presence of strong radiative damping. Table 1 enumerates all the simulations presented here.

3. RESULTS OF THE 2D RUNS

In this section, we present and discuss the results of the 2D runs listed in Table 1. After describing the overall time evolution of the reconnection layers in the xy - and yz -planes (Section 3.1), we present a Fourier analysis of the tearing and kink instabilities as a function of the guide field strength (Section 3.2). Then, we deduce from the particle and photon spectra the most/least favorable conditions for particle accelera-

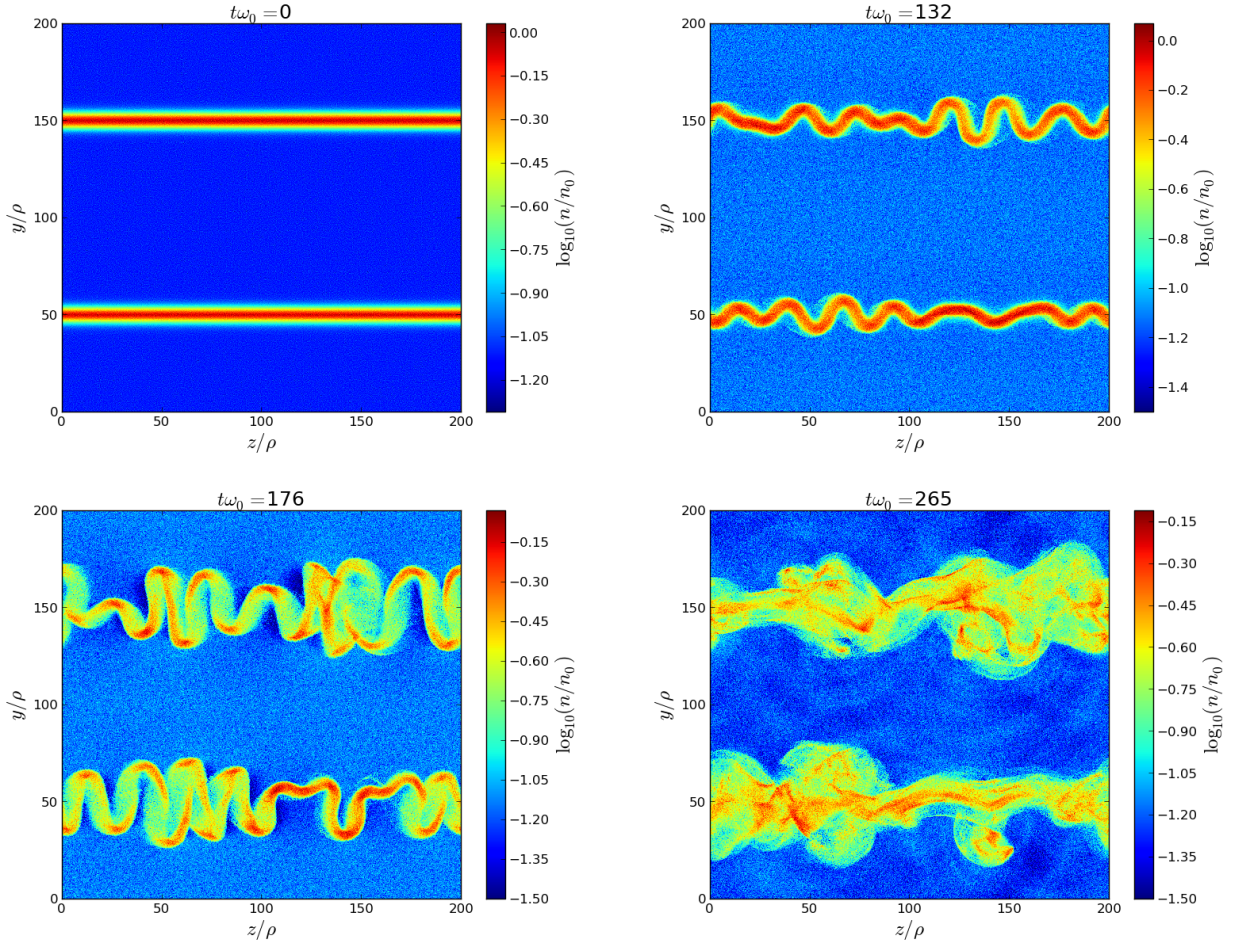


FIG. 3.— Snapshot of the plasma density at $t\omega_0 = 0$ (top left), 132 (top right), 176 (bottom left), and 265 (bottom right) of the 2D simulation 2DYZ0 in the yz -plane (with no guide field, $\alpha = 0$). Although this simulation cannot capture magnetic reconnection that proceeds in the xy -plane, it shows that the layers rapidly destabilize along the z -direction due to the kink instability. The layers are deformed and eventually completely disrupted, leading to efficient dissipation of the magnetic energy (about 55%), mostly in the form of heat (see Figures 6-8).

tion beyond γ_{rad} and synchrotron emission > 160 MeV in 3D (Section 3.3).

3.1. Description of the time evolution

Figure 2 shows the time evolution of the total plasma density and field lines at four characteristic stages of 2D magnetic reconnection in the xy -plane with $\alpha = 0$ (run 2DXY0). Because there is no initial perturbation, the layers remain static until $t\omega_0 \approx 120$ when the layer tears apart into about 7 plasmoids per layer separated by X-points where field lines reconnect. The noise of the macro-particles in the PIC code is sufficient to seed the tearing instability. The reconnection electric field E_z is maximum at X-points and is responsible for most of particle acceleration. The high magnetic tension of freshly reconnected field lines pushes the plasma towards the $\pm x$ -directions and drives the large scale reconnection outflow that forces magnetic islands to merge with each other. Reconnection proceeds until there is only one big island per layer remaining in the box. At the end of the simulation ($t\omega_0 = 353$), about 70% of the initial magnetic energy is dissipated in the form of particle kinetic energy. All the energy gained by the particles is then lost via the emission of synchrotron radiation. Adding a guide field does not suppress the tearing instability, but it creates a charge separation across the layer that induces a strong E_y electric field (see also Zenitani & Hoshino 2008;

Cerutti et al. 2013).

Figure 3 presents the time evolution of the 2D simulation in the yz -plane with no guide field (run 2DYZ0). The initial setup of fields and particles is identical to run 2DXY0, except that the reconnecting field (B_x) is now perpendicular to the simulation plane. Hence, reconnection and tearing modes cannot be captured by this simulation. Instead, we observe the development of the kink instability as early as $t\omega_0 \approx 100$ in the form of a small sinusoidal deformation of the current sheets with respect to the initial layer mid-plane. The sinusoidal deformation proceeds along the z -direction, with the deformation amplitude in the y -direction increasing rapidly up to about a quarter of the simulation box size (about $50\rho_0$). At this stage, the folded current layers are disrupted, leading to fast and efficient magnetic dissipation. About 55% of the total magnetic energy is dissipated by the end of the simulation. The guide field has a dramatic influence on the stability of the layers. The amplitude of the deformation as well as the magnetic energy dissipated decreases with increasing guide field. For $\alpha \gtrsim 0.75$, the layers remain flat during the entire duration of the simulation and no magnetic energy is dissipated. In this case, the only noticeable time evolution is a slight decrease of the layer thickness due to synchrotron cooling. To maintain pressure balance across the layers with the unchanged upstream magnetic field, the layer must com-

press to compensate for the radiative energy losses (Uzdensky & McKinney 2011). We observed also a compression of the reconnection layer in the xy -reconnection simulations.

3.2. Fourier analysis of unstable modes

To compare the relative strength of the tearing instability versus the kink instability, we perform a spectral analysis of the fastest growing modes that develop in the simulations. To study the kink instability, we do a fast Fourier transform (FFT) along the z -direction of the small variations of the reconnecting magnetic field in the bottom layer mid-plane, $\delta B_x(z, t) = B_x(y = L_y/4, z, t) - B_x(y = L_y/4, z, 0)$, during the early phase of the 2D simulations in the yz -plane. For the tearing modes, we follow the same procedure for the fluctuations in the reconnected field along the x -direction, $\delta B_y(x, t) = B_y(x, y = L_y/4, t) - B_y(x, y = L_y/4, 0)$, in the 2D simulations in the xy -plane.

We present in Figure 4 the time evolution of the fastest growing modes as well as the dispersion relations for the tearing and kink modes, with no guide field. In the linear regime ($t\omega_0 \lesssim 125$), we infer the growth rates by fitting the amplitude of each mode with $|\text{FFT}(\delta B_{x,y}/B_0)| \propto \exp(\gamma_{\text{gr}}(k)t)$, where γ_{gr} is the growth rate of the mode of wave-number k . We find that the fastest growing tearing mode is at $k_x\delta \approx 0.58$, which coincides with the analytical expectation of $k_x\delta = 1/\sqrt{3}$ (Zelenyi & Krasnoselskikh 1979) as found by Zenitani & Hoshino (2007). The wavelength of this mode is $L_x/\lambda_x = L_x/2\pi\sqrt{3}\delta \approx 7$; this explains the number of plasmoids formed in the early stages of reconnection (see top right panel in Figure 2). The fastest growing kink mode has a wavelength $L_z/\lambda_z \approx 8$ (or $k_z\delta \approx 0.67$) which is consistent with the deformation of the current layers observed in Figure 3, top right panel. The corresponding growth rate is $\gamma_{\text{KI}}\omega_0^{-1} \approx 0.055$, which is comparable with the fastest tearing growth rate, $\gamma_{\text{TI}}\omega_0^{-1} \approx 0.045$ (Figure 4, bottom panel). This is expected for an ultra-relativistic plasma ($kT \gg m_e c^2$) with a drift velocity $\beta_{\text{drift}} = 0.6$ (Zenitani & Hoshino 2007). It is worth noting that the dispersion relations for both the kink and the tearing instabilities are not sharply peaked around the fastest growing modes; a broad range of low-frequency modes is almost equally unstable (i.e., for $0 < k_{x,z}\delta \lesssim 1$).

In agreement with Zenitani & Hoshino (2008) and as pointed out in Section 3.1, we find that the kink instability depends sensitively on the guide field strength. Figure 5 shows that the fastest growth rate decreases rapidly between $\alpha = 0.25$ and $\alpha = 0.75$ from $\gamma_{\text{KI}}\omega_0^{-1} \approx 0.055$ to undetectable levels. Thus, the guide field stabilizes the layer along the z -direction. In contrast, as mentioned earlier in Section 3.1, the tearing growth rate depends only mildly on α ; we note a decrease from $\gamma_{\text{TI}}\omega_0^{-1} \approx 0.045$ for $\alpha = 0$ to $\gamma_{\text{TI}}\omega_0^{-1} \approx 0.025$ for $\alpha = 1$. For $\alpha \gtrsim 0.5$, the tearing instability dominates over the kink.

3.3. Particle and photon spectra

The critical quantities of interest here are the particle energy distributions, $\gamma^2 dN/d\gamma$, and the instantaneous optically thin synchrotron radiation spectral energy distribution (SED) emitted by the particles, $\nu F_\nu \equiv E^2 dN_{\text{ph}}/dt dE$, where E is the photon energy. Figure 6 shows the time evolution of the total particle spectra at different times with no guide field in the xy -plane (top panel) and in the yz -plane (bottom panel). In the early stage ($t\omega_0 \lesssim 132$), both simulations are subject to

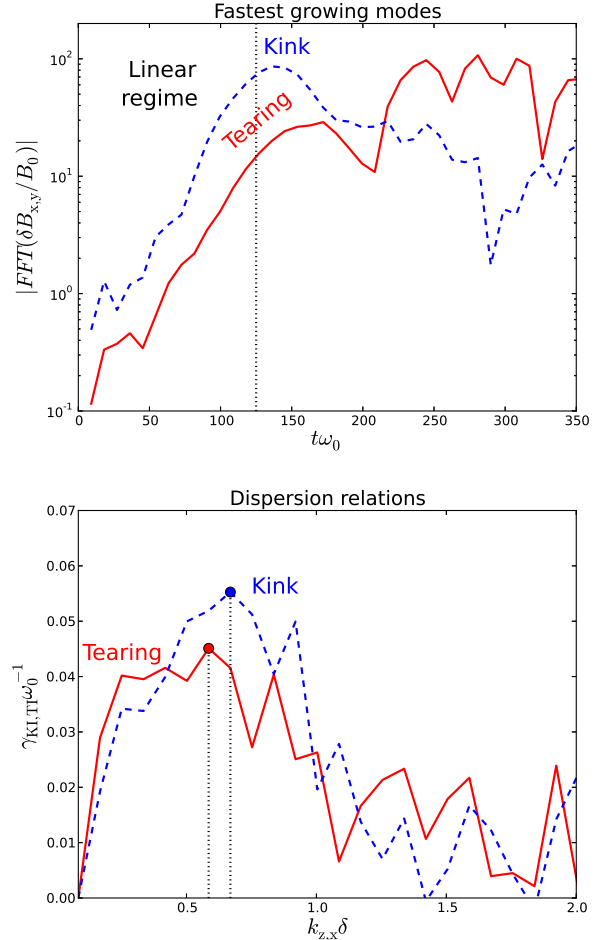


FIG. 4.— Top: Time evolution of the fastest growing tearing (red solid line, $k_x\delta \approx 0.58$) and kink (blue dashed line, $k_z\delta \approx 0.67$) modes, in the simulation 2DXY0 and 2DYZ0 where $\alpha = 0$. The duration of the linear phase is $t\omega_0 \approx 125$ (delimited by the vertical dotted line) and is about the same in both simulations. Bottom: Dispersion relations of the tearing (red solid line) and kink (blue dashed line) instabilities during the linear stage. This plot shows only the region of small wavenumber $k_{z,x}$ where the most unstable modes are found. The vertical black dotted lines mark the fastest growing modes.

pure synchrotron cooling (i.e., with no acceleration or heating) of the plasma that results in a decrease of the typical Lorentz factor of the particles from $\gamma/\gamma_{\text{rad}} \approx 0.3$ at $t\omega_0 = 0$ to $\gamma/\gamma_{\text{rad}} \approx 0.08$ at $t\omega_0 = 132$. The decrease of the mean particle energy within the layer explains the shrinking of the layer thickness described in Section 3.1.

At $t\omega_0 \gtrsim 132$, the instabilities trigger magnetic dissipation and particles are energized, but the particle spectra differ significantly in both cases. In run 2DXY0, where the tearing instability drives reconnection, the particle spectrum extends to higher and higher energy with time until the end of the simulation, where the maximum energy reaches $\gamma_{\text{max}}/\gamma_{\text{rad}} \approx 2.5$, i.e., well above the nominal radiation reaction limit. The spectrum above $\gamma/\gamma_{\text{rad}} = 0.1$ cannot be simply modeled with a single power-law, but it is well contained between two steep power laws of index -2 and -3 . We know from our previous study that the high-energy particles are accelerated via the reconnection electric field at X-points and follow relativistic Speiser orbits (Cerutti et al. 2013). The maximum energy is then given by the electric potential drop along the z -direction

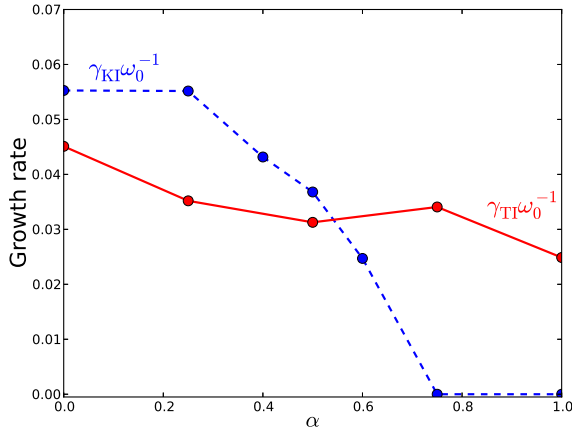


FIG. 5.— Linear growth rates of the fastest growing modes for the tearing (for $\gamma_{\text{TI}}(k_x = 0.58)$, red solid line) and the kink (for $\gamma_{\text{KI}}(k_z = 0.67)$, blue dashed line) instabilities multiplied by ω_0^{-1} , as a function of the guide field strength α . Each dot represents one simulation. The analysis of the kink/tearing instability was performed using the set of 2D simulations in the yz - xy -plane.

(neglecting radiative losses), i.e.,

$$\gamma_{\text{max}} \sim \frac{eE_z L_x}{m_e c^2} = \frac{e\beta_{\text{rec}} B_0 L_x}{m_e c^2} \approx 3\gamma_{\text{rad}}, \quad (6)$$

for a dimensionless reconnection rate $\beta_{\text{rec}} \approx 0.2$. Particles above the radiation reaction limit ($\gamma > \gamma_{\text{rad}}$) account for about 5% of the total energy of the plasma at $t\omega_0 = 318$ (Figure 7, top panel), and are responsible for the emission of synchrotron radiation above 160 MeV. Figure 7 (bottom panel) shows the resulting isotropic synchrotron radiation SED at $t\omega_0 = 318$, where about 11% of the radiative power is > 160 MeV. The SED peaks at $E = 10$ MeV and extends with a power-law of index -0.42 up to about 300-400 MeV before cutting off exponentially.

In contrast, in run 2DYZ0, where the kink instability drives the annihilation of the magnetic field, the particles are heated up to a typical energy $\gamma/\gamma_{\text{rad}} \approx 0.3$. The particle spectrum is composed of a Maxwellian-like distribution on top of a cooled distribution of particles formed at $t\omega_0 \lesssim 132$ (Figures 6, 8). The mean energy of the hot particles corresponds to a nearly uniform redistribution of the total dissipated magnetic energy to kinetic energy of background particles, i.e.,

$$\langle \gamma \rangle \sim 0.55 \times \frac{B_0^2/8\pi}{(0.1n_0)m_e c^2} = 0.55 \times \frac{\sigma\theta_0}{2} \approx 0.34\gamma_{\text{rad}}, \quad (7)$$

where the numerical factor 0.55 accounts for the fraction of the total magnetic energy dissipated at the end of the simulation. Hence, the development of the kink prevents the acceleration of particles above γ_{rad} and the emission of synchrotron photons above 160 MeV. Figure 8 (bottom panel) shows that the total synchrotron radiation SED peaks and cuts off at $E = 10$ MeV, far below the desired energies > 160 MeV.

Because a moderate guide field suppresses the effect of the kink instability, hence magnetic dissipation, the particles are not heated for $\alpha \gtrsim 0.5$, and the initial spectrum continues cooling until the end of the yz -plane simulation where the particles radiate low-energy (~ 1 MeV) synchrotron radiation (Figure 8). In the xy -plane reconnection simulations, the guide field tends to decrease the maximum energy of the particles and of the emitted radiation (Figure 7, see also Cerutti

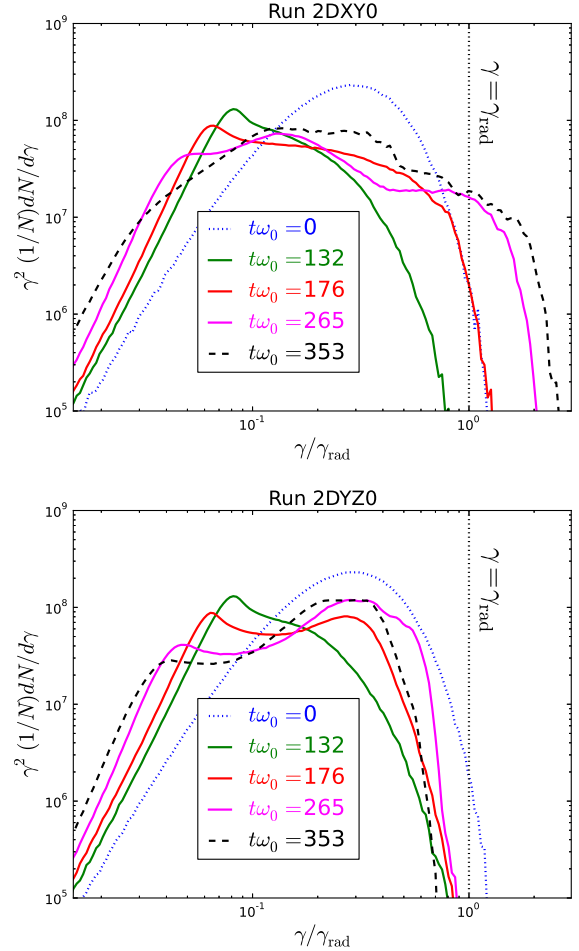


FIG. 6.— Particle energy distribution normalized to the total number of particles ($\gamma^2(1/N)dN/d\gamma$) of the 2D simulations in the xy -plane (top, run 2DXY0) and yz -plane (bottom, run 2DYZ0) for $\alpha = 0$. The spectra are obtained at time $t\omega_0 = 0$ (dotted line), 132, 176, 265 and 353 (dashed line) and are averaged over all directions. The particle Lorentz factor is normalized to the nominal radiation reaction limit $\gamma_{\text{rad}} \approx 1.3 \times 10^9$.

et al. 2013). The guide field deflects the particles outside the layer, reducing the time spent by the particle within the accelerating region.

4. RESULTS OF THE 3D RUNS

From the previous section, we find that the tearing and kink modes grow at a similar rate and wavelength in our setup. Both instabilities lead to fast dissipation of the magnetic energy in the form of thermal and non-thermal particles. The kink instability tends to disrupt the layer, which prevents non-thermal particle acceleration and emission above the standard radiation reaction limit. It is desirable to impose a moderate guide field to diminish the negative effect of the kink on particle acceleration, but too strong a guide field is not advantageous either, as it decreases the maximum energy reached by the particles and radiation. Hence, we decided to run a 3D simulation with an $\alpha = 0.5$ guide field (run 3D050, see Table 1), which appears to be a good compromise. For comparison, we also performed a 3D simulation without guide field (run 3D0). In this section, we first describe the time evolution of 3D reconnection in the two runs (Section 4.1). Then, we provide a quantitative analysis of the most unstable modes in the $(k_x \times k_z)$ -plane in the linear regime (Sec-

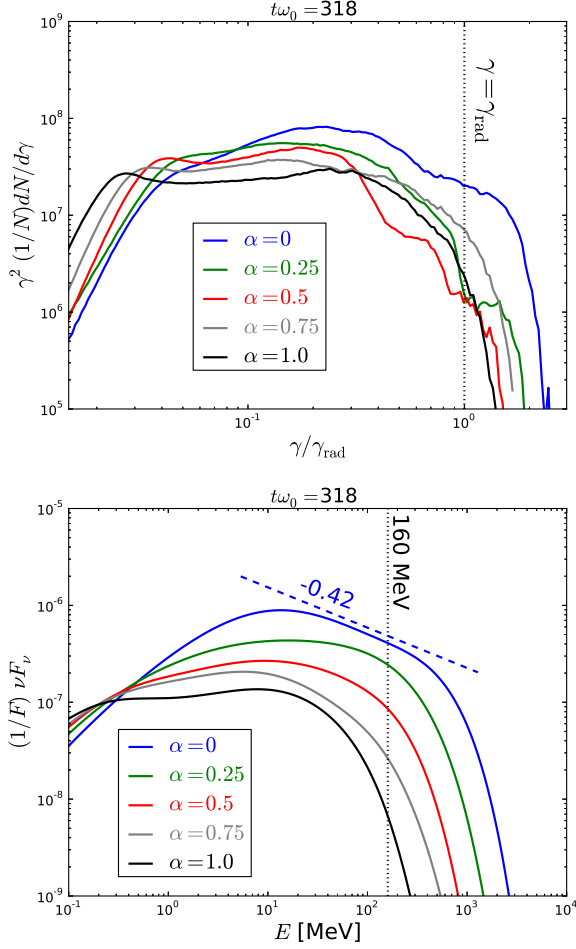


FIG. 7.— Particle energy distribution normalized to the total number of particles ($\gamma^2(1/N)dN/d\gamma$, top) and synchrotron radiation spectral distribution normalized by the total (frequency-integrated) photon flux ($(1/F)\nu F_\nu$, bottom) of the 2D simulations in the xy -plane at $t\omega_0 = 318$, averaged over all directions. The spectra are obtained for $\alpha = 0, 0.25, 0.5, 0.75$ and 1 . The particle Lorentz factor in the top panel is normalized to the nominal radiation reaction limit $\gamma_{\text{rad}} \approx 1.3 \times 10^9$. In the bottom panel, the blue dashed line is a power-law fit of index ≈ -0.42 of the $\alpha = 0$ SED between $E = 20$ MeV and $E = 350$ MeV.

tion 4.2). In addition, we address below the question of particle acceleration, emission (Section 4.3), particle and radiation anisotropies (Section 4.4), the expected radiative signatures (i.e., spectra and lightcurves) and comparison with the *Fermi-LAT* observations of the Crab flares (Sections 4.5, 4.6).

4.1. Plasma time evolution

Figure 9 (left panels) shows the time evolution of the plasma density³ in the zero-guide field simulation at $t\omega_0 = 0, 173, 211$ and 269 . The initial stage where the layer remains apparently static lasts for about $t\omega_0 = 144$, i.e., half of the whole simulation time. At $t\omega_0 \gtrsim 144$, overdensities appear in the layers in the form of 7-8 tubes (flux ropes) elongated along the z -direction. These structures are generated by the tearing instability and are the 3D generalization of the magnetic islands observed in 2D reconnection. As the simulation proceeds into the non-linear regime, the flux ropes merge with each other creating bigger ones, as magnetic islands do in 2D

³ Movies are available at this URL: http://benoit.cerutti.free.fr/movies/Reconnection_Crab3D/.

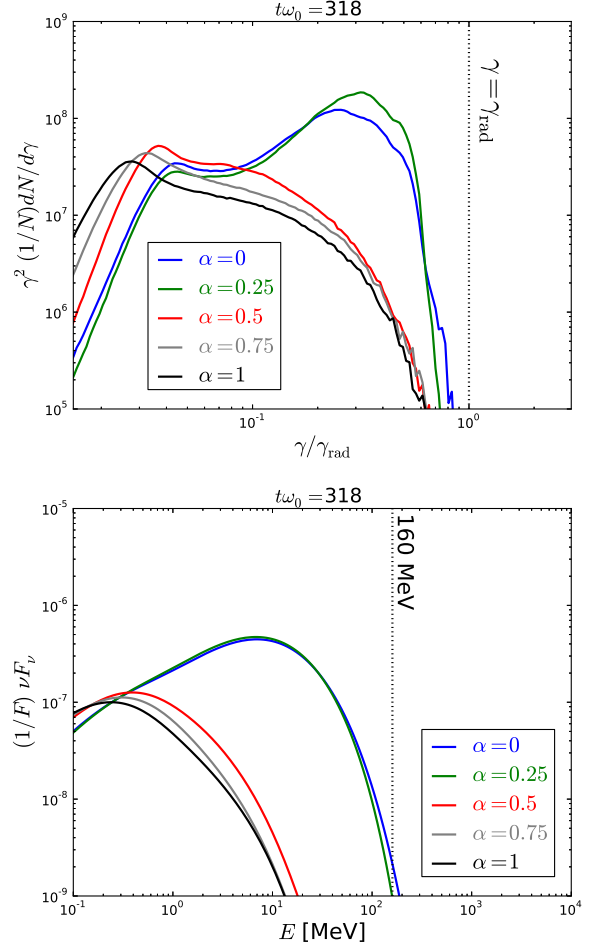


FIG. 8.— Same as in Figure 7, but for the 2D simulations in the yz -plane.

reconnection. However, in 3D this process does not happen at the same time everywhere along the z -direction, which results in the formation of a network of interconnected flux ropes at intermediate times ($173 \lesssim t\omega_0 \lesssim 211$).

In parallel to this process, the kink instability deforms the two layers along the z -direction in the form of sine-like translation of the layers' mid-planes in the $\pm y$ -directions. During the most active period of reconnection ($t\omega_0 \gtrsim 173$), the kink instability takes over and eventually destroys the flux ropes formed by the tearing modes (see left bottom panel in Figure 9). Only a few coherent structures survive at the end of the simulation ($t\omega_0 = 269$). In particular the reconnection electric field, which is strongest along the X-lines between two flux ropes, loses its initial coherence. This results in efficient particle heating but poor particle acceleration (see below, Section 4.3). At the end of this run about 52% of the total magnetic energy is dissipated, although the simulation does not reach the fully saturated state.

The right panels in Figure 9 shows the time evolution of the plasma density for $\alpha = 0.5$ guide field. One sees immediately that the guide field effectively suppresses the kink deformations of the layers in the $\pm y$ -directions, as expected from the 2D simulations in the yz -plane (See Section 3) and from Zenitani & Hoshino (2008). In contrast, the tearing instability seems undisturbed and breaks the layer into a network of 8 flux tubes. Towards the end of the simulation, there are about 3 well-defined flux ropes containing almost all the plasma that

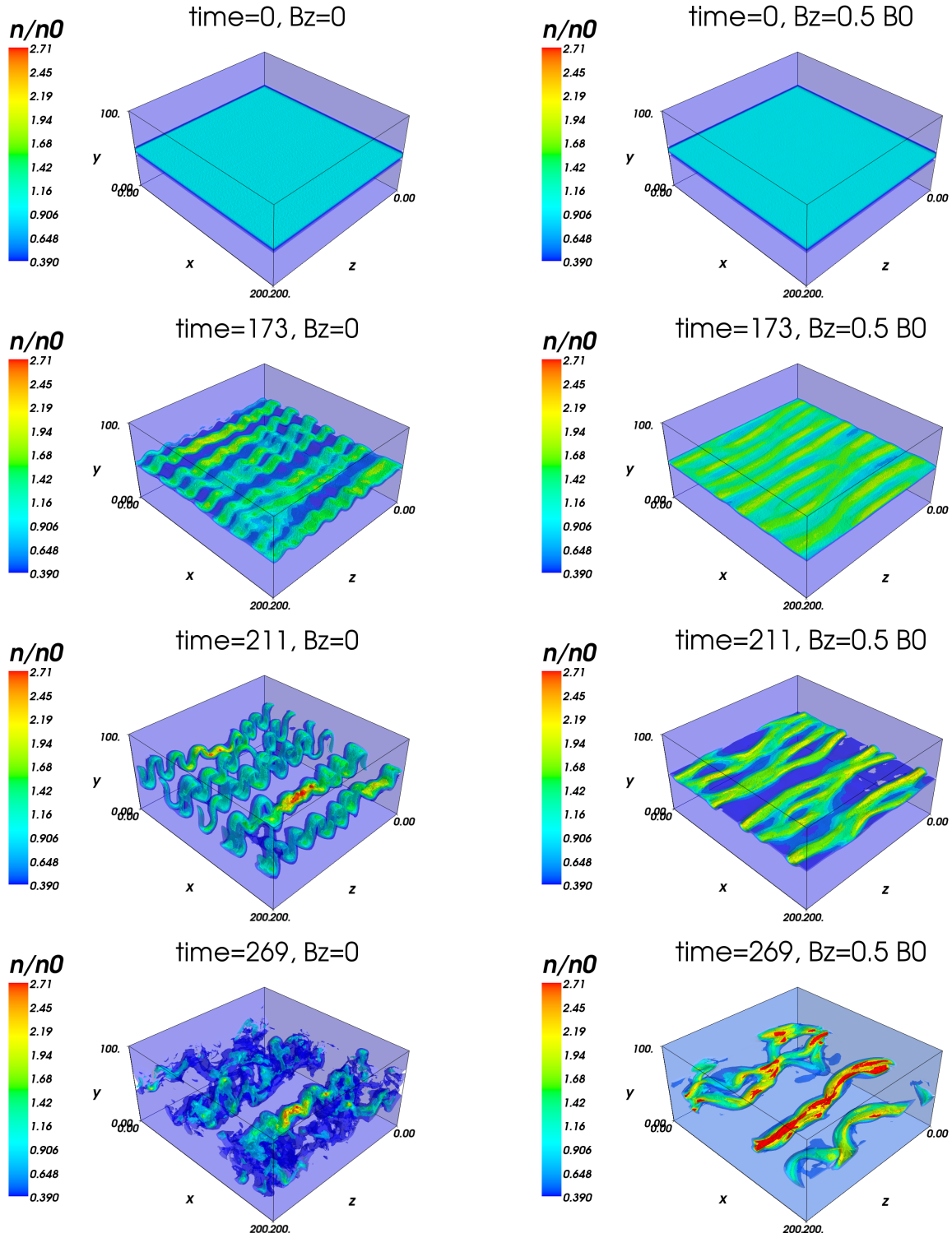


FIG. 9.— Time evolution of the plasma density (color-coded isosurfaces) in the bottom half of the simulation box at $t\omega_0 = 0, 173, 211,$ and 269 (from top to bottom), for $\alpha = 0$ (left panels, run 3D0) and $\alpha = 0.5$ (right panels, run 3D050). Low-density isosurfaces (blue) are transparent in order to see the high-density regions (red) nested in the flux tubes. The time is given in units of ω_0^{-1} , and spatial coordinates are in units of ρ_0 .

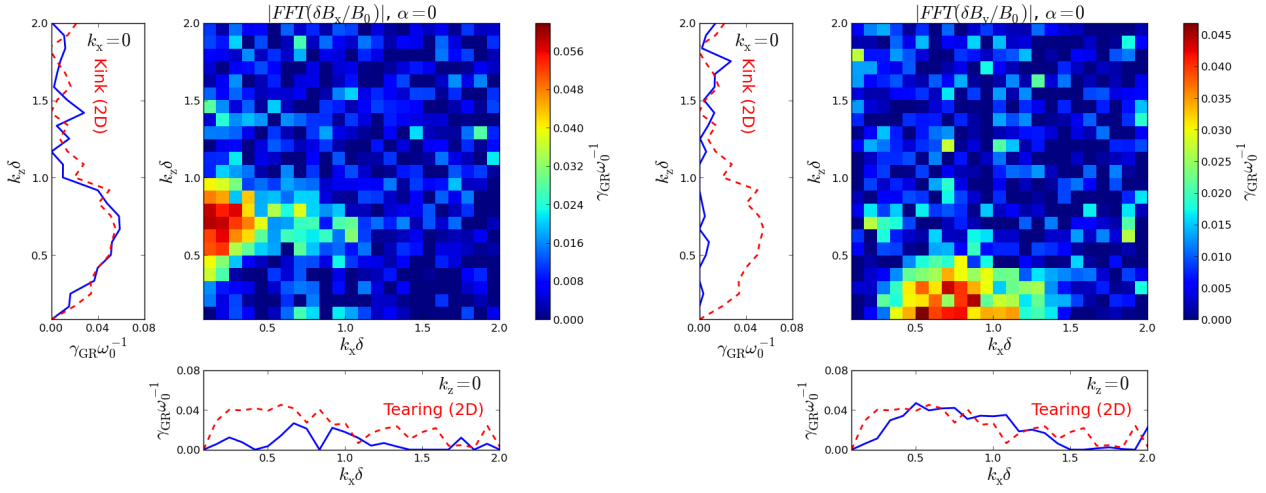


FIG. 10.— Linear growth rates in run 3D0 γ_{GR} times ω_0^{-1} in the $(k_x \times k_z)$ -plane (color-coded plots) using the fluctuations in B_x (left panel) which are most sensitive to kink-like modes, and in B_y (right panel) which are most sensitive to tearing-like modes. The blue solid lines in each subplot give the growth rates along the k_x -axis for $k_z = 0$ (bottom subplots) and along the k_z -axis for $k_x = 0$ (left subplots). The red dashed lines show the dispersion relation for the pure kink and tearing modes obtained in Section 3.2 for comparison.

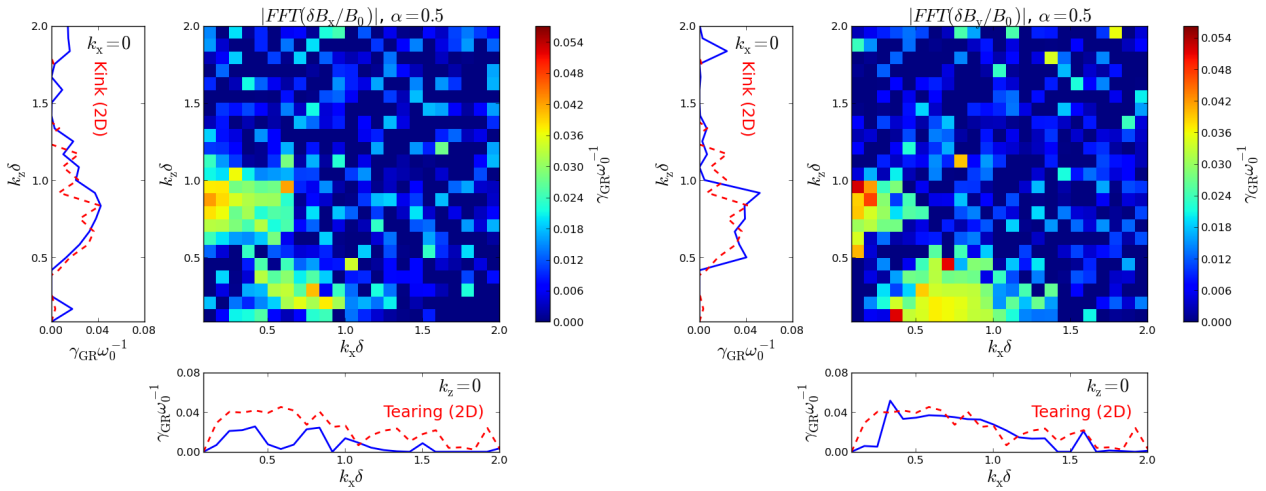


FIG. 11.— Same as in Fig. 10 with an $\alpha = 0.5$ guide field (run 3D050).

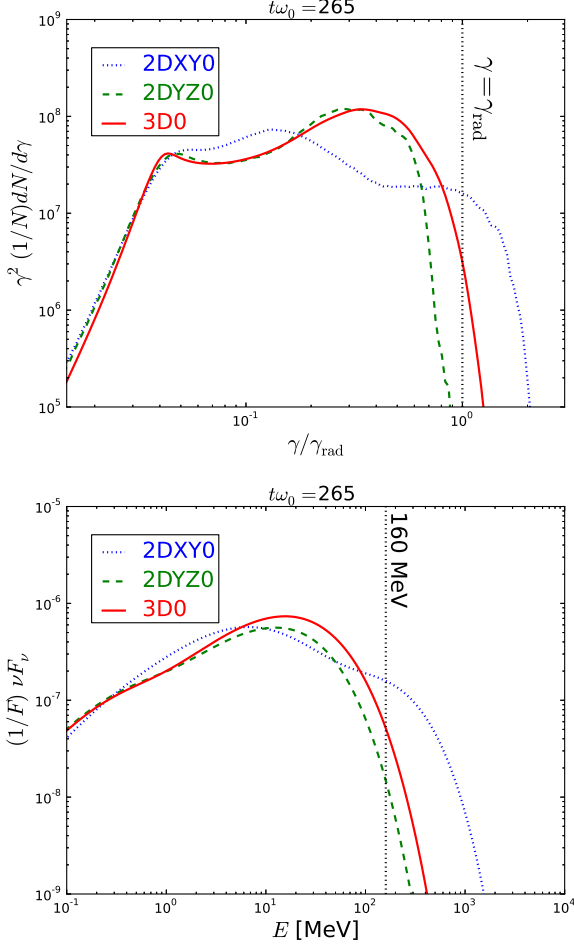


FIG. 12.— Isotropically averaged particle energy distribution (top panel) and SED (bottom panel) obtained in 2D (xy -plane, blue dotted line, and in the yz -plane, green dashed line) and 3D (red solid line) with no guide field.

went through reconnection. At this point in time, 20% of the total magnetic energy (i.e., including the reconnecting and the guide field energy) has dissipated, in agreement with the 2D run 2DXY050.

4.2. Fourier analysis of unstable modes

Following the analysis presented in Section 3.2, we perform a Fourier decomposition of the magnetic fluctuations in the bottom layer mid-plane, ($x, y = L_y/4, z$), to study the most unstable modes that develop in the 3D simulations. Figure 10 presents the growth rate of each mode in the ($k_x \times k_z$)-plane estimated from the variations of B_x (left panel) and B_y (right panel), for $\alpha = 0$. As pointed out in Section 3.2 and by Zenitani & Hoshino (2008) and Kagan et al. (2013), we find that the reconnecting field B_x effectively captures the kink-like modes along k_z whereas the reconnected field B_y is most sensitive to tearing-like modes along k_x . The dispersion relations show that pure kink (along k_z for $k_x = 0$) and pure tearing (along k_x for $k_z = 0$) modes grow at rates in very good agreement with the corresponding 2D simulations. With a growth rate $\gamma_{GR} \approx 0.06\omega_0$, the fastest growing mode in the simulation is a pure kink mode of wavenumber $k_z\delta \approx 0.7$, or $L_z/\lambda_z \approx 8$ consistent with the deformation of the layer observed in the earlier stage of reconnection (Figure 9, left panels) and with the 2D run 2DYZ0. The fastest tearing mode has a growth rate $\gamma_{GR} \approx 0.045\omega_0$ at $k_x\delta \approx 0.5$ and generates the ≈ 7 ini-

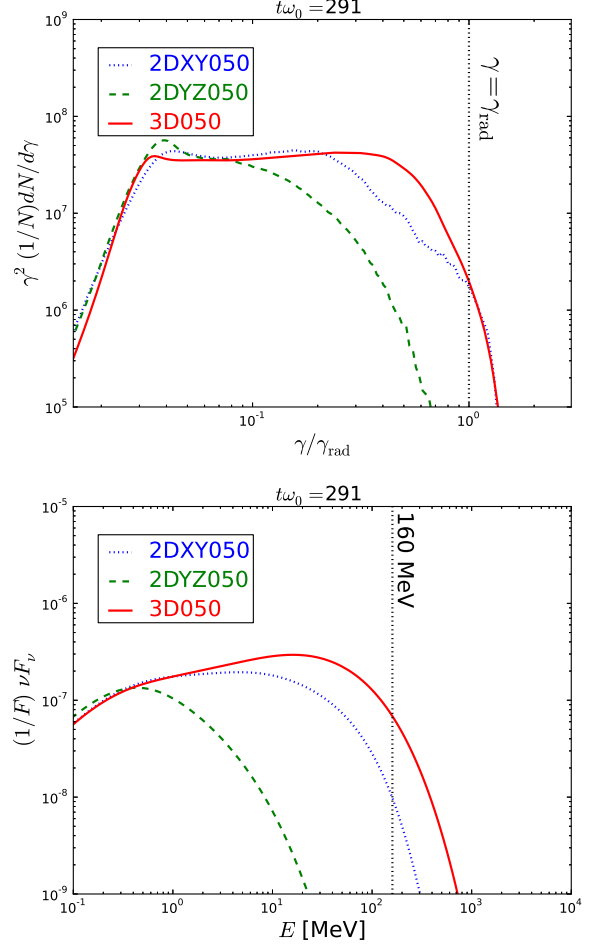


FIG. 13.— Same as in Figure 12, but with an $\alpha = 0.5$ guide field.

tial flux ropes obtained in the simulation. The ($k_x \times k_z$)-plane is also filled with oblique modes, i.e., waves with a non-zero k_x - and k_z -component, with growth rates comparable to the fastest tearing and kink modes. The existence of these modes is reflected by the flux ropes being slightly tilted in the xz -plane. Adding an $\alpha = 0.5$ guide field decreases the amplitude of the low-frequency ($k_z\delta \lesssim 1$) growth rates of the kink modes (Figure 11). In particular, the growth rate of the fastest mode for $\alpha = 0$, $k_z\delta = 0.7$, decreases from $0.06\omega_0$ to $0.03\omega_0$. As a result, the fastest growing kink mode is now at $k_z\delta = 0.8$ with a rate $\approx 0.04\omega_0$, while the fastest growing tearing modes is approximately unchanged, in excellent agreement with the 2D runs (Figure 11).

4.3. Particle and photon spectra

Figure 12 presents the particle and photon energy distributions averaged over all directions at $t\omega_0 = 265$, with no guide field. The distributions are remarkably similar to the 2D run 2DYZ0 ones, and differ significantly from run 2DXY0. The high-energy part of the particle spectrum peaks at $\gamma/\gamma_{rad} = 0.3$ which is the signature of particle heating via magnetic dissipation rather than particle acceleration through tearing-dominated reconnection (Section 3.3, Eq. 7). We note that the spectrum extends to higher energy than the pure magnetic dissipation scenario, slightly above γ_{rad} , suggesting that there is a non-thermal component as well. On the contrary, in the $\alpha = 0.5$ guide field case (run 3DG050, Figure 13),

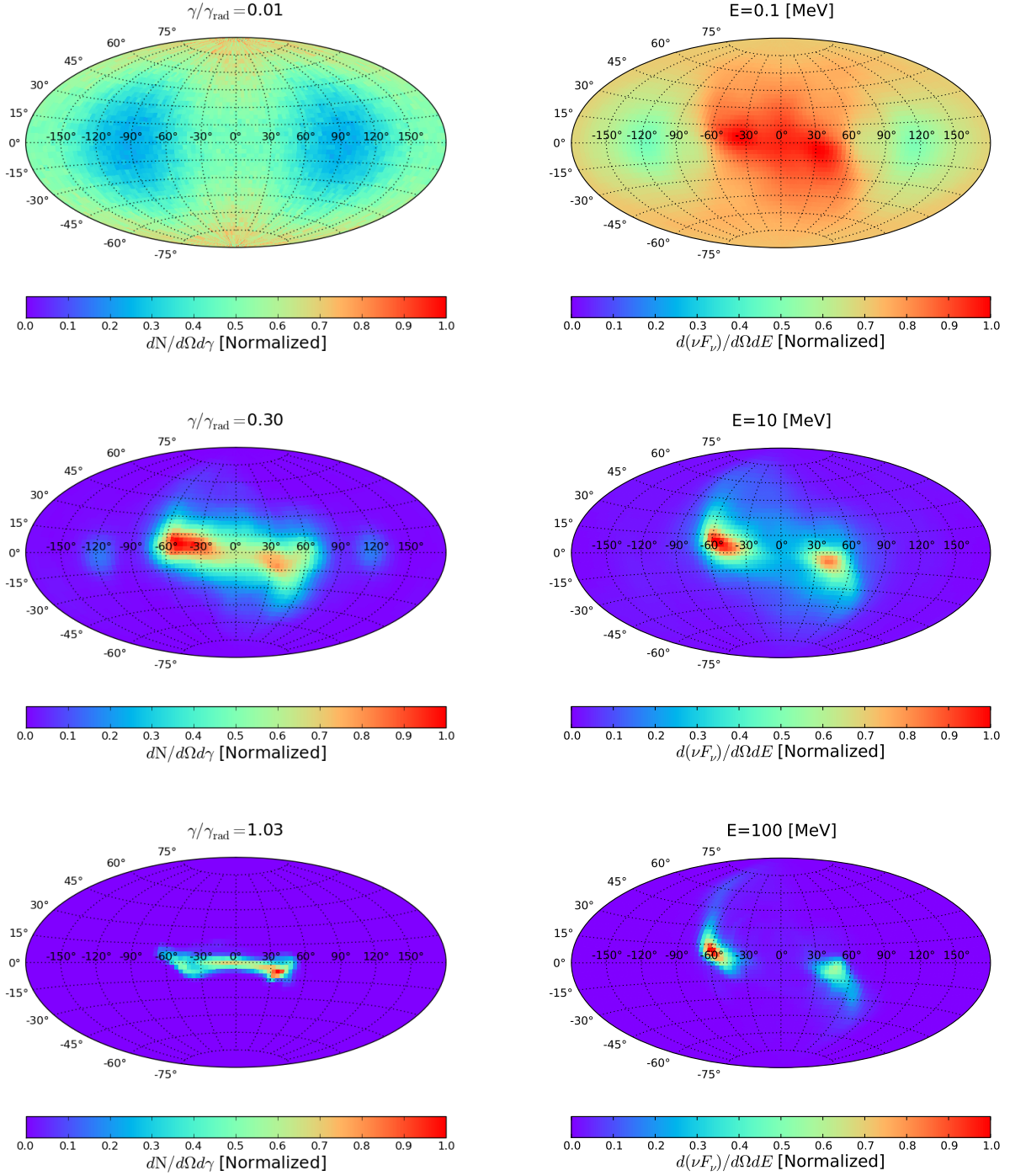


FIG. 14.— Positron angular distributions ($dN/d\Omega d\gamma$, left panels) and their synchrotron radiation angular distribution ($d(\nu F_\nu)/d\Omega dE$, right panels) in run 3D050 ($\alpha = 0.5$) at $t\omega_0 = 291$. Each panel is at a different energy bin: $\gamma/\gamma_{\text{rad}} = 0.01$ (top left), 0.3 (middle left) and 1 (bottom left) for the particles and $E = 0.1$ MeV (top right) 10 MeV (middle right) and 100 MeV (bottom right) for the photons. The color-coded scale is linear and normalized to the maximum value in each energy bin. The angular distribution is shown in the Aitoff projection, where the horizontal-axis is the longitude, λ , varying between $\pm 180^\circ$ ($-z$ -axis) and the vertical axis is the latitude, ϕ , varying between -90° ($-y$ -direction) to $+90^\circ$ ($+y$ -direction). The origin of the plot corresponds to the $+z$ -direction.

things are closer to the pure tearing reconnection case of run 2DX050. The particle energy distribution is almost flat in the $0.04 \lesssim \gamma/\gamma_{\text{rad}} \lesssim 0.4$ range, but barely reaches above γ_{rad} as in the zero-guide field case. Nevertheless, the synchrotron emission > 160 MeV is more intense than in the zero guide field case. Even though there is clear evidence for particle acceleration above the radiation reaction limit, the effect remains slightly weaker than in 2D with no guide field. A bigger box size would help to improve the significance of this result.

4.4. Particle and photon anisotropies

The angular distribution of the particles is of critical interest for determining the apparent isotropic radiation flux seen by a distant observer who probes one direction only. In 2D reconnection, we expect a pronounced beaming of the particles that increases rapidly with their energy (Cerutti et al. 2012b, 2013). We confirm here that this phenomenon exists also in 3D, even with a finite guide field. Figure 14 presents energy-resolved maps of the angular distribution of the positrons (left panels) and their optically thin synchrotron radiation (right panel) in run 3D050. The direction of motion of the particles is measured with two angles: the latitude, ϕ , varying between -90° and 90° , defined as

$$\phi = \sin^{-1} \left(\frac{u_y}{\sqrt{u_x^2 + u_y^2 + u_z^2}} \right), \quad (8)$$

and the longitude, λ , defined between -180° and 180° given by

$$\lambda = \begin{cases} \cos^{-1} \left(\frac{u_z}{\sqrt{u_x^2 + u_z^2}} \right) & \text{if } \sin \lambda > 0 \\ -\cos^{-1} \left(\frac{u_z}{\sqrt{u_x^2 + u_z^2}} \right) & \text{if } \sin \lambda < 0 \end{cases}, \quad (9)$$

where u_x , u_y , and u_z are the components of the particle 4-velocity vector.

We find that the low-energy particles ($\gamma/\gamma_{\text{rad}} \lesssim 0.1$) nearly conserve the initially imposed isotropy, because they are still upstream and have not been energized by reconnection. In contrast, the high-energy particles ($\gamma/\gamma_{\text{rad}} \gtrsim 0.1$) are significantly beamed along the reconnection plane (at X-lines and with flux ropes) within $\phi = \pm 15^\circ$ and $\lambda = \pm 60^\circ$. The $\lambda = \pm 60^\circ$ angle is of special interest here because it coincides with the direction of the undisturbed magnetic field lines outside the reconnection layers for a $\alpha = 0.5$ guide field ($\lambda_0 = \pm \tan^{-1}(1/\alpha) \approx \pm 63^\circ$). The particles are accelerated along the z -direction by the reconnection electric field, and move back and forth across the layer mid-plane following relativistic Speiser orbits (Cerutti et al. 2013). At the same time, the particles are deflected away by the reconnected field and the guide field creating a characteristic ‘‘S’’ shape in the angular maps. To a lesser extent, the zero-guide field case also presents some degree of anisotropy, but the deformation and then the disruption of the layer by the kink instability effectively broaden the beams.

The synchrotron angular distribution closely follows the particle one, essentially because relativistic particles radiate along their direction of motion within a cone of semi-aperture angle $\sim 1/\gamma \ll 1$. However, there is a noticeable offset between the distribution of the highest-energy particles with $\gamma \gtrsim \gamma_{\text{rad}}$ and the radiation above 100 MeV. This discrepancy is due to the different zones where particles accelerate and

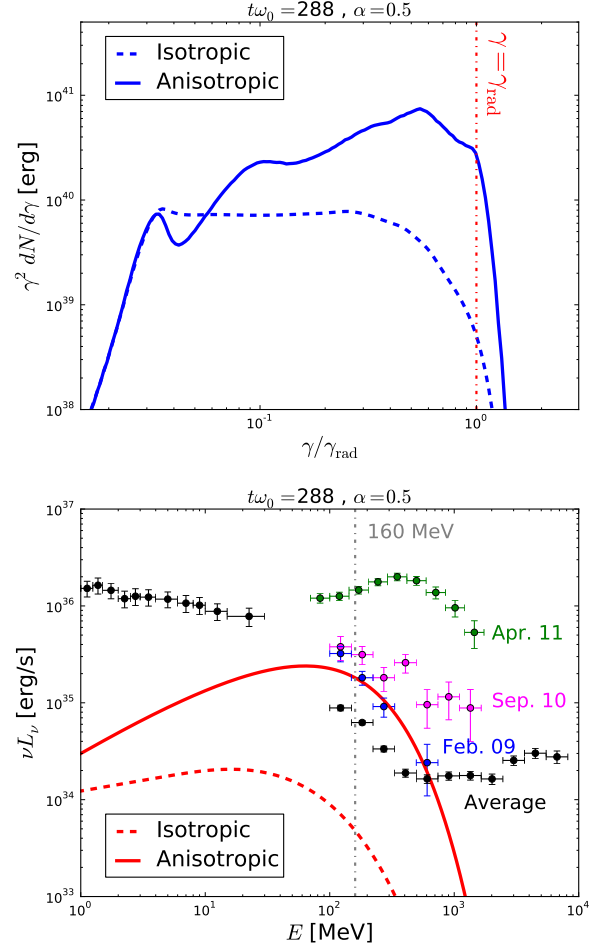


FIG. 15.— Top: Comparison between the isotropically averaged particle energy distribution (dashed line) and the apparent isotropic distribution in the $\phi = -9.2^\circ$, $\lambda = 34.5^\circ$ direction (solid line). Bottom: Comparison between the isotropically averaged synchrotron SED (dashed line), the apparent isotropic SED in the $\phi = 5.5^\circ$, $\lambda = -63.6^\circ$ direction at $t\omega_0 = 288$, for $\alpha = 0.5$ (solid line), and the observed *Fermi*-LAT spectra (data points) during the flares in February 2009, September 2010, and in April 2011, as well as the average quiescent spectrum from 1 MeV to 10 GeV (Abdo et al. 2011; Buehler et al. 2012). Observed fluxes are converted into isotropic luminosities, assuming that the nebula is at 2 kpc from Earth.

where particles radiate. In the accelerating zone, the electric field is intense and leads to linear particle acceleration along the z -axis, whereas the perpendicular magnetic field, B_\perp , is weak deep inside the reconnection layers, yielding little synchrotron radiation. These high-energy particles then radiate $\gtrsim 100$ MeV emission abruptly, i.e., within a fraction of a Larmor gyration, only when they are deflected outside the layer where $B_\perp \sim B_0$. The beam dump is well localized at $\lambda = \pm 60^\circ$, i.e., along the upstream magnetic field lines (see hot-spots in Figure 14, bottom-right panel).

4.5. Apparent spectra and comparison with observations

As a consequence of this strong anisotropy, the observed spectra of particles and radiation depend sensitively on the viewing angle. Figure 15 compares the isotropic particle (top panel) and photon energy distributions (apparent intrinsic isotropic luminosities, νL_ν , bottom panel) with the distributions along one of the directions dominated by the highest energy particles ($\phi = -9.2^\circ$, $\lambda = 34.5^\circ$) and radiation ($\phi = 5.5^\circ$, $\lambda = -63.6^\circ$) as it appears to a distant observer at

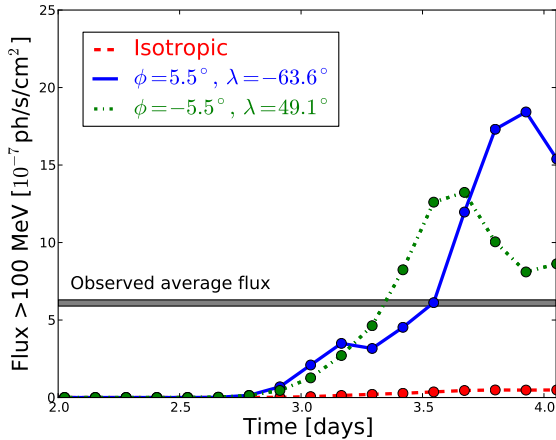


FIG. 16.— Instantaneous synchrotron photon flux integrated above 100 MeV as a function of time in the directions $\phi = 5.5^\circ$, $\lambda = -63.6^\circ$ (blue solid line), $\phi = -5.5^\circ$, $\lambda = 49.1^\circ$ (green dot-dashed line), and isotropically averaged (red dotted line) in run 3D050. Fluxes are given in ph/s/cm^2 , assuming a distance of 2 kpc between the layer and the observer. The horizontal gray band shows the average observed flux of the Crab Nebula above 100 MeV measured by the *Fermi*-LAT, equal to $6.1 \pm 0.2 \times 10^{-7} \text{ ph/s/cm}^2$ (Buehler et al. 2012).

$t\omega_0 = 288$, for $\alpha = 0.5$ (see Section 4.4 and Figure 14). The bottom panel in Figure 15 also compares the *Fermi*-LAT measurements of the gamma-ray spectra of the February 2009, September 2010 and April 2011 flares and the average quiescent spectrum of the Crab Nebula (Abdo et al. 2011; Buehler et al. 2012) with the simulated gamma-ray spectra. The particle spectrum in the ($\phi = -9.2^\circ$, $\lambda = 34.5^\circ$) direction is very hard, and peaks at $\gamma/\gamma_{\text{rad}} \approx 0.6$ with a total apparent isotropic energy $\approx 7 \times 10^{40}$ erg, which corresponds to about half the total magnetic energy dissipated by the end of the simulation, or about 10 times more energy than in the isotropic distribution. The photon spectrum in the ($\phi = 5.5^\circ$, $\lambda = -63.6^\circ$) direction peaks at about 100 MeV but extends up to ~ 1 GeV. The resulting gamma-ray luminosity above 100 MeV is $L_\gamma \approx 3 \times 10^{35}$ erg/s, which is about 40 times brighter than the isotropically averaged flux from the layer, and about 3 times brighter than the observed average (quiescent) luminosity of the Crab Nebula ($L_{\gamma}^{\text{Crab}} \approx 10^{35}$ erg/s, assuming a distance of 2 kpc between the nebula and the observer). Thanks to beaming, the level of gamma rays expected from the model is consistent with the moderately bright flares, such as the February 2009 or September 2010 ones (see Figure 15, bottom panel), but the simulation cannot reproduce the flux of the brightest flares, such as the April 2011 event. Presumably, increasing the box size would be enough to increase the density of the emitting particles > 100 MeV and account for the most intense flares.

4.6. Lightcurves

The beam of high-energy radiation is also time variable, both in direction and in intensity. Figure 16 presents the computed time evolution of the synchrotron photon flux integrated above 100 MeV in the directions defined by $\phi = 5.5^\circ$, $\lambda = -63.6^\circ$ and $\phi = -5.5^\circ$, $\lambda = 49.1^\circ$, as well as the computed time evolution of the isotropically-averaged flux and the observed average flux in the Crab Nebula measured by the *Fermi*-LAT (Buehler et al. 2012) for comparison. This calculation assumes that all the photons emitted at a given instant throughout the box reach the observer at the same time,

i.e., it ignores the time delay between photons emitted in different regions with respect to the observer. Along the directions probed here, the > 100 MeV flux doubling timescale is of order $10 - 20\omega_0^{-1}$ or 3-6 hours, for both the rising and the decaying time, which is compatible with the observations of the Crab flares (Buehler et al. 2012; Mayer et al. 2013), as well as with our previous 2D simulations in Cerutti et al. (2013). Shorter variability timescales may still exist in the simulation but our measurement is limited by the data dumping period set at $T_{\text{dump}} \approx 10\omega_0^{-1}$. These synthetic lightcurves also clearly illustrate the effect of the particle beaming on the observed flux discussed in Section 4.5. Along the direction of the beam, the > 100 MeV flux can be $\gtrsim 10$ times more intense than the isotropically-averaged one, and even exceeds the measured quiescent gamma-ray flux of the Crab Nebula by a factor $\approx 2-3$ at the peak of the lightcurves 3.5 to 4 days after the beginning of the simulation. Each time the beam crosses our line of sight, we see a rapid bright flare of the most energetic radiation emitted in the simulation.

The high-energy particles are strongly bunched within the magnetic flux ropes (within magnetic islands in 2D, see Cerutti et al. 2012b, 2013). As a result, the typical size of the emitting regions is comparable to the dimensions of the flux ropes, i.e., of order $L_x/10 \approx 20\rho_0$ along the x - and y -directions (Figure 9), which corresponds to about 6 light-hours. We conclude that particle bunching is at the origin of the ultra-short time variability (3-6 hours) found in the reconstructed lightcurve (Figure 16). Particle bunching and anisotropy help to alleviate the severe energetic constraints imposed by the Crab flares.

5. CONCLUSION

We found that, unlike classical models of particle acceleration, 3D relativistic pair plasma reconnection can accelerate particles above the standard radiation reaction limit in the Crab Nebula. We also confirm the existence of a strong energy-dependent anisotropy of the particles and their radiation, resulting in an apparent boosting of the high-energy radiation observed when the beam crosses our line of sight. In this case, the simulated gamma-ray flux > 100 MeV exceeds the measured quiescent flux from the nebula by a factor 2-3, and reproduces well the flux of moderately bright flares, such as the February 2009 or the September 2010 events. Simulating brighter flares (e.g., the April 2011 flare) may be achieved with a larger box size. In addition, the bunching of the energetic particles within the magnetic flux ropes results in rapid time variations of the observed gamma-ray flux ($\lesssim 6$ hours). The results are consistent with observations of the Crab flares and with our previous 2D simulations (Cerutti et al. 2013), although this extreme acceleration is less pronounced than in 2D due to the deformation of the layer by the kink instability in 3D. If there is no guide field, we found that the kink instability grows faster than the tearing instability, resulting in the disruption of the reconnection layers and significant particle heating rather than reconnection and non-thermal particle acceleration. In agreement with Zenitani & Hoshino (2007, 2008), we observe that a moderate guide field ($\alpha \sim 0.5$) is enough to reduce the negative effect of the kink on the acceleration of particles. However, a strong guide field (i.e., $\alpha \gtrsim 1$) quenches particle acceleration and the emission of high-energy emission because it deflects the particles away from the X-lines too rapidly.

Applying a guide field is probably not the only way to suppress kink instability. In the Harris configuration, an initial

ultra-relativistic drifting particle flow (with $\beta_{\text{drift}} \gtrsim 0.6$) is expected to foster tearing-dominated reconnection (Zenitani & Hoshino 2007) as observed by Liu et al. (2011). Alternatively, starting with an out-of-equilibrium layer could also drive a fast onset of reconnection (Kagan et al. 2013). In real systems, the reconnection layer is not likely to be smooth, flat, undisturbed, and in equilibrium. A small perturbation in the field lines, like a pre-existing X-point, can favor fast reconnection before the kink instability has time to grow. Hence, while we have shown one set of conditions emitting > 160 MeV radiation, there may be other conditions allowing reconnection to produce similar results.

The reconnection model could be refined if future multi-wavelength observations can pin down the location of the flares in the Crab Nebula (so far there is nothing obvious, see e.g., Weisskopf et al. 2013). One promising location for reconnection-powered flares could be within the jets in the polar regions where the plasma is expected to be highly magnetized (i.e., $\sigma \gtrsim 1$) with stronger magnetic field close to the pulsar rotational axis (Uzdensky et al. 2011; Cerutti et al. 2012a; Lyubarsky 2012; Komissarov 2013; Mignone et al. 2013; Porth et al. 2013b). In addition, theoretical studies (Begelman 1998), numerical simulations (Mizuno et al. 2011; Porth et al. 2013a,b; Mignone et al. 2013), and possibly X-ray observations (Weisskopf 2011) indicate that the jets are unstable to kink instabilities. The non-linear development of these instabilities could lead to the formation of current sheets, presumably with a non-zero guide field, and then to magnetic dissipation in the Crab Nebula in the form of powerful gamma-ray flares, which may contribute to solving the “ σ -problem” in pulsar wind nebulae (Rees & Gunn 1974; Kennel & Coroniti 1984).

Relativistic reconnection may also be at the origin of other astrophysical flares. Most notably, TeV gamma-ray flares observed in blazars (e.g., Aharonian et al. 2007; Albert et al. 2007; Aleksić et al. 2011) present challenges similar to the Crab flares (e.g., ultra-short time variability, problematic energetics) that could be solved by invoking relativistic reconnection in a highly magnetized jet (Giannios et al. 2009, 2010;

Nalewajko et al. 2011, 2012; Cerutti et al. 2012b; Giannios 2013). The physical conditions in blazar jets are quite different than in the Crab Nebula (e.g., composition, inverse Compton drag, pair creation), which may change the dynamics of reconnection. The current sheet that forms beyond the light-cylinder in pulsars offers another interesting environment for studying relativistic reconnection subject to strong synchrotron cooling. Pairs energized by reconnection may be at the origin of the GeV pulsed emission in gamma-ray pulsars (Lyubarskii 1996; Pétri 2012; Uzdensky & Spitkovsky 2012; Arka & Dubus 2013). We speculate that synchrotron radiation from the particles could even account for the recently reported > 100 GeV pulsed emission from the Crab (see, e.g., VERITAS Collaboration et al. 2011; Aleksić et al. 2012) if particle acceleration above the radiation reaction limit operates in this context.

BC thanks G. Lesur for discussions about the linear analysis of the unstable modes in the simulations. The authors thank the referee for his/her useful comments. BC acknowledges support from the Lyman Spitzer Jr. Fellowship awarded by the Department of Astrophysical Sciences at Princeton University, and the Max-Planck/Princeton Center for Plasma Physics. This work was also supported by NSF grant PHY-0903851, DOE Grants de-sc0008409 and de-sc0008655, NASA grant NNX12AP17G through the Fermi Guest Investigator Program. Numerical simulations were performed on the local CIPS computer cluster Verus and on Kraken at the National Institute for Computational Sciences (www.nics.tennessee.edu/). This work also utilized the Janus supercomputer, which is supported by the National Science Foundation (award number CNS-0821794), the University of Colorado Boulder, the University of Colorado Denver, and the National Center for Atmospheric Research. The Janus supercomputer is operated by the University of Colorado Boulder. The figures published in this work were created with the `matplotlib` library (Hunter 2007) and the 3D visualization with `Mayavi2` (Ramachandran & Varoquaux 2011).

REFERENCES

- Abdo, A. A., Ackermann, M., Ajello, M., et al. 2011, *Science*, 331, 739
 Aharonian, F. A., et al. 2007, *ApJ*, 664, L71
 Albert, J., et al. 2007, *ApJ*, 669, 862
 Aleksić, J., et al. 2011, *ApJ*, 730, L8
 Aleksić, J., et al. 2012, *A&A*, 540, A69
 Arka, I., & Dubus, G. 2013, *A&A*, 550, A101
 Arons, J. 2012, *Space Sci. Rev.*, 173, 341
 Balbo, M., Walter, R., Ferrigno, C., & Bortas, P. 2011, *A&A*, 527, L4
 Begelman, M. C. 1998, *ApJ*, 493, 291
 Birdsall, C. K., & Langdon, A. B. 2005, *Plasma physics via computer simulation* (New York: Taylor & Francis)
 Blandford, R., & Eichler, D. 1987, *Phys. Rep.*, 154, 1
 Buehler, R., Scargle, J. D., Blandford, R. D., et al. 2012, *ApJ*, 749, 26
 Buehler, R., & Blandford, R. D. 2013, *Reports on Progress in Physics*, [arXiv:1309.7046](https://arxiv.org/abs/1309.7046)
 Buson, S., Buehler, R., & Hays, E. 2013, *ATel*, 5485
 Capdessus, R., d’Humières, E., & Tikhonchuk, V. T. 2012, *Phys. Rev. E*, 86, 036401
 Cerutti, B., Uzdensky, D. A., & Begelman, M. C. 2012, *ApJ*, 746, 148
 Cerutti, B., Werner, G. R., Uzdensky, D. A., & Begelman, M. C. 2012, *ApJ*, 754, L33
 Cerutti, B., Werner, G. R., Uzdensky, D. A., & Begelman, M. C. 2013, *ApJ*, 770, 147
 Contopoulos, I. 2007, *A&A*, 472, 219
 Daughton, W., Roytershteyn, V., Karimabadi, H., et al. 2011, *Nature Physics*, 7, 539
 de Jager, O. C., Harding, A. K., Michelson, P. F., et al. 1996, *ApJ*, 457, 253
 Giannios, D., Uzdensky, D. A., & Begelman, M. C. 2009, *MNRAS*, 395, L29
 Giannios, D., Uzdensky, D. A., & Begelman, M. C. 2010, *MNRAS*, 402, 1649
 Giannios, D. 2013, *MNRAS*, 431, 355
 Guilbert, P. W., Fabian, A. C., & Rees, M. J. 1983, *MNRAS*, 205, 593
 Hunter, J. D. 2007, *Computing in Science & Engineering*, 9, 90
 Jaroschek, C. H., & Hoshino, M. 2009, *Phys. Rev. Lett.*, 103, 075002
 Kagan, D., Milosavljevic, M., & Spitkovsky, A. 2013, 774, 41
 Kennel, C. F., & Coroniti, F. V., *ApJ*, 283, 694
 Kirk, J. G., & Skjæraasen, O. 2003, *ApJ*, 591, 366
 Kirk, J. G. 2004, *Phys. Rev. Lett.*, 92, 181101
 Kirk, J. G., Lyubarsky, Y., & Petri, J. 2009, in *Neutron Stars and Pulsars*, ed. W. Becker (Astrophysics and Space Science Library, Vol. 357; Berlin: Springer), 421
 Komissarov, S. S. 2013, *MNRAS*, 428, 2459
 Landau, L. D., & Lifshitz, E. M. 1975, *The Classical Theory of Fields* (Oxford: Pergamon Press)
 Liu, W., Li, H., Yin, L., Albright, B. J., Bowers, K. J., & Liang, E. P. 2011, *Phys. Plasmas*, 18, 052105
 Lyubarskii, Y. E. 1996, *A&A*, 311, 172
 Lyubarsky, Y. E. 2012, *MNRAS*, 427, 1497
 Lyutikov, M. 2010, *MNRAS*, 405, 1809
 Markidis, S., Henri, P., Lapenta, G., et al. 2013, *Phys. Plasmas*, 20, 082105
 Meyer, M., Horns, D., & Zechlin, H.-S. 2010, *A&A*, 523, A2

- Mayer, M., Buehler, R., Hays, E., et al. 2013, *ApJ*, 775, L37
- Mignone, A., Striani, E., Tavani, M., & Ferrari, A. 2013, [arXiv:1309.0375](https://arxiv.org/abs/1309.0375)
- Mizuno, Y., Lyubarsky, Y., Nishikawa, K.-I., & Hardee, P. E. 2011, *ApJ*, 728, 90
- Nalewajko, K., Giannios, D., Begelman, M. C., Uzdensky, D. A., & Sikora, M. 2011, *MNRAS*, 413, 333
- Nalewajko, K., Begelman, M. C., Cerutti, B., Uzdensky, D. A., & Sikora, M. 2012, *MNRAS*, 425, 2519
- Parker, E. N. 1957, *J. Geophys. Res.*, 62, 509
- Pétri, J. 2012, *MNRAS*, 424, 2023
- Porth, O., Komissarov, S. S., & Keppens, R. 2013, *MNRAS*, 431, L48
- Porth, O., Komissarov, S. S., & Keppens, R. 2013, [arXiv:1310.2531](https://arxiv.org/abs/1310.2531)
- Ramachandran, P., & Varoquaux, G. 2011, *Computing in Science & Engineering*, 13, 40
- Rees, M. J., & Gunn, J. E. 1974, *MNRAS*, 167, 1
- Sironi, L., & Spitkovsky, A. 2011, *ApJ*, 741, 39
- Speiser, T. W. 1965, *J. Geophys. Res.*, 70, 4219
- Striani, E., Tavani, M., Piano, G., et al. 2011, *ApJ*, 741, L5
- Striani, E., Tavani, M., Vittorini, V., et al. 2013, *ApJ*, 765, 52
- Sweet, P. A. 1958, in *IAU Symp. 6, Electromagnetic Phenomena in Cosmical Physics*, ed. B. Lehnert (Cambridge: Cambridge Univ. Press), 123
- Tamburini, M., Pegoraro, F., Di Piazza, A., Keitel, C. H., & Macchi, A. 2010, *New J. Phys.*, 12, 123005
- Tavani, M., Bulgarelli, A., Vittorini, V., et al. 2011, *Science*, 331, 736
- Uzdensky, D. A., & McKinney, J. C. 2011, *Phys. Plasmas*, 18, 042105
- Uzdensky, D. A., Cerutti, B., & Begelman, M. C. 2011, *ApJ*, 737, L40
- Uzdensky, D. A., & Spitkovsky, A. 2012, [arXiv: 1210.3346](https://arxiv.org/abs/1210.3346)
- VERITAS Collaboration, Aliu, E., Arlen, T., et al. 2011, *Science*, 334, 69
- Weisskopf, M. 2011, [arXiv:1111.3315](https://arxiv.org/abs/1111.3315)
- Weisskopf, M. C., Tennant, A. F., Arons, J., et al. 2013, *ApJ*, 765, 56
- Yee, K. 1966, *IEEE Trans. Antennas Propagat.*, 14, 302
- Zelenyi, L. M., & Krasnoselskikh, V. V. 1979, *Soviet Astronomy*, 23, 460
- Zenitani, S., & Hoshino, M. 2005, *PhRvL*, 95, 095001
- Zenitani, S., & Hoshino, M. 2007, *ApJ*, 670, 702
- Zenitani, S., & Hoshino, M. 2008, *ApJ*, 677, 530
- Zweibel, E. G., & Yamada, M. 2009, *ARA&A*, 47, 291